In-ho Lee
Department of Naval Architecture and
Marine Engineering,
University of Michigan,
1231 Beal Avenue,
2010 Walter E. Lay Automotive Laboratory,
Ann Arbor, MI 48109
e-mail: leeinho@umich.edu

Simo A. Mäkiharju
Mem. ASME
Department of Naval Architecture and
Marine Engineering,
University of Michigan,
1085 S. University Avenue,
126B West Hall,
Ann Arbor, MI 48109
e-mail: smakihar@umich.edu

Harish Ganesh
Department of Mechanical Engineering,
University of Michigan,
1231 Beal Avenue,
2010 Walter E. Lay Automotive Laboratory,
Ann Arbor, MI 48109
e-mail: gharish@umich.edu

Steven L. Ceccio
Mem. ASME
Department of Naval Architecture and
Marine Engineering,
University of Michigan,
2600 Draper Drive,
Naval Architecture and Marine
Engineering Building,
Ann Arbor, MI 48109
e-mail: ceccio@umich.edu

Scaling of Gas Diffusion Into Limited Partial Cavities

Bubbles populations in the wake of a partial cavity resulting from gas diffusion were measured to determine the noncondensable gas flux into the cavity. The diffusion rate is related to the dissolved gas content, the local cavity pressure, and the flow within and around the cavity. The measurements are used to revisit various scaling relationships for the gas diffusion, and it is found that traditional scaling that assumes the presence of a gas pocket overpredicts the gas diffusion. A new scaling based on diffusion into the low void fraction bubbly mixture within the partial cavity is proposed, and it is shown to adequately scale the observed production of gas bubbles for dissolved air saturation from 30% to 70% at 1 atm, limited cavities on the order of 0.3–3 cm in length at a free-stream speed of 8 m/s ($\sigma = 2.3$–3.3 and Reynolds number based on the cavity length of order 10^5). [DOI: 10.1115/1.4031850]

Introduction

Small noncondensable gas bubbles are typically present in the wake of partial cavitation. Partial cavitation is often associated with a low-pressure region of flow separation that is either partially or fully filled with the fluid's vapor phase. If the freestream liquid contains dissolved gas, some of this gas may diffuse into the cavity at the low-pressure liquid–vapor interfaces. Entrainment and pressure recovery in the cavity wake leads to condensation of the vapor, but the noncondensable gas may not rapidly return to solution. Instead, clouds of small gas bubbles will be convected away from the cavity. This process was discussed by a number of previous researchers, including the authors of Refs. [1–5]. A review presented by Yu and Ceccio [6] used measurements of the bubble populations downstream of a partial cavity to compare the observed gas diffusion rates to those predicted from four different scaling models.

Figure 1(*a*) shows a schematic diagram of an ideal partial cavity, adapted from Yu and Ceccio [6]. Here, it is assumed that the gas pocket is at vapor pressure. The freestream speed, cavitation number, and dissolved noncondensable gas content are U, σ, and c_O, respectively. The flow velocity at the cavity free surface is $U_C = U\sqrt{1+\sigma}$, and the length is L_C. At the cavity surface, the saturated dissolved gas content is c_S. The turbulent boundary layer over the cavity interface is characterized with a boundary layer thickness, δ, and momentum thickness, θ. Gas diffusion rates into the cavity can then written as

$$\dot{m}_B = k_B(c_O - c_S)U_C L_D W \tag{1}$$

where k_B is a constant, L_D is a length scale derived from modeling assumptions, and W is the span. Based on the different models of Refs. [2,5,7], L_D takes different forms as shown below.

If molecular diffusion is the dominant mechanism [5], then

$$L_{\mathrm{DPK}} = \sqrt{DL_C/U_C} \tag{2}$$

where D is the molecular mass diffusion coefficient and $k_B = 2.25$. This model corresponds to a Schmidt number, $S_C = \upsilon/D$, at the cavity interface of zero (e.g., mass transport occurs solely by molecular diffusion), where υ is the liquid kinematic viscosity. For turbulent diffusion at the cavity interface with a turbulent $S_{C_t} = \upsilon/D_t = 1$, where D_t is the turbulent diffusivity, Brennen predicted that

$$L_{\mathrm{DB}} = \sqrt{L_C\theta} \tag{3}$$

with $k_B = 0.45$. Similarly, Parkin and Ravindra [7] modified their laminar diffusion model by employing a turbulent diffusivity

$$L_{\mathrm{DPR}} = \sqrt{L_C\delta} \tag{4}$$

Contributed by the Fluids Engineering Division of ASME for publication in the Journal of Fluids Engineering. Manuscript received November 17, 2014; final manuscript received October 15, 2015; published online January 4, 2016. Assoc. Editor: Olivier Coutier-Delgosha.

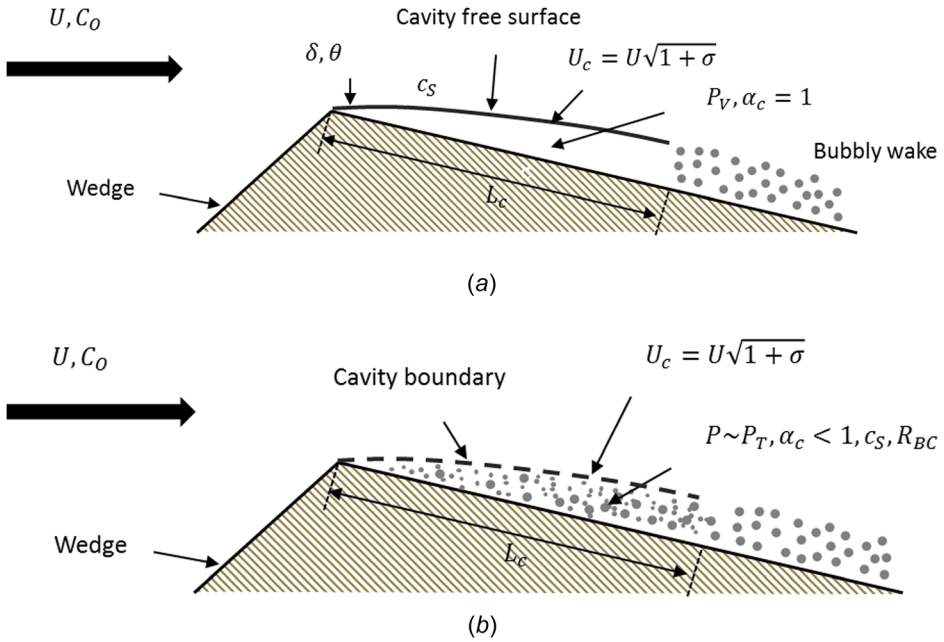

Fig. 1 Schematic drawings of the partial cavity flows: (*a*) the classical depiction of the cavity as a vapor pocket with a free surface and (*b*) representation of the cavity as a bubbly mixture

with $k_B = 0.18$. Note that since $\theta \approx \delta/10$ for a developed turbulent boundary layer, the modified Parkin model and the Brennen model are nearly equivalent. Finally, if we assume that the turbulent Schmidt number is very large, $S_{C_t} = \upsilon/D_t \gg 1$, we can derive the slug flow model

$$L_{\mathrm{DSF}} = \delta \tag{5}$$

with $k_B = 1$. We assume here that all the gas in the boundary layer above the cavity rapidly enters the cavity.

Yu and Ceccio [6] measured diffusion-produced bubble populations downstream of a stable partial cavity, computed the gas flux, and compared the observed and predicted gas flux [6]. They found that the molecular diffusion model significantly underestimated the gas flux, as expected. But the models that assumed turbulent mass diffusion at the cavity boundary overestimated the rate of gas diffusion by at least two orders of magnitude. Subsequent to these measurements, researchers have shown that the void fraction in partial cavities can vary widely, ranging from a few percent gas-fraction to near unity [8,9].

In the present work, we revisit the gas diffusion scaling with a new set of measurements that include the volume fraction of the cavitating region, α_C. Figure 1(*b*) illustrates the flow around a partial cavity that is comprised of a bubbly mixture with $0 < \alpha_C < 1$. The void fraction and static pressure within the separated cavity may vary, and there is liquid flow into and out of the cavity. Hence, we will propose a new scaling that considers the gas diffusion that can take place within the bubbly mixture. For this scaling, we base the cavity size on a size of a 5% void fraction contour, and for simplicity, the bubble size and pressure are taken to be constant within this contour. We then compare the measured and predicted gas diffusion rates using previous and newly developed scaling.

Experimental Setup

The experiments were performed in the University of Michigan's 9-inch Water Tunnel, and a modified test section with a working cross section of 7.62×7.62 cm was used to facilitate X-ray measurements. Limited partial cavities in water were created at the apex of a wedge, placed in a square test section of a water channel (as shown in Fig. 2). The flow speed and pressure in the reduced test section can be independently controlled. The incoming average flow speed, U, was set at 8 ± 0.2 m/s. The flow speed near the cavity interface, just downstream of the wedge apex where the cavity formed (the throat speed), estimated from the inlet flow speed is $U_C = 12 \pm 0.3$ m/s. The freestream static pressure, P, was measured with a Omega Engineering, PX20-030A5V, 0–207 kPa, absolute pressure transducer with manufacturer stated accuracy of 0.08% of full scale (i.e., 170 Pa). The pressure transducer was varied to change the freestream cavitation number

$$\sigma = \frac{P - P_V}{\frac{1}{2}\rho U^2} \tag{6}$$

where P_V is the liquid vapor pressure and ρ is the liquid density. The uncertainty in the cavitation number is ± 0.2. The freestream temperature was in the range of $24 \pm 1\,^{\circ}\mathrm{C}$.

A deaeration system was used to change the dissolved gas content of liquid flow. The dissolved oxygen (DO) content of the freestream flow, c_0, was measured using a DO meter (Thermo Scientific Orion Star, Thermo-Scientific) to an uncertainty of $\pm 2\%$. As discussed by Yu and Ceccio [6], the DO content is related, but not equivalent, to the dissolved air content of the flow. However, we will assume that the percentage of dissolved oxygen saturation is similar to the percentage of dissolved total air concentration, and that the ppm of nitrogen is 1.8 that of oxygen, which is an approximation discussed by Yu and Ceccio [6]. From this, we can determine the level of saturation at various pressures with Henry's law constant for air such that for a given pressure (at $24\,^{\circ}\mathrm{C}$) $c_S = (0.223 \pm 0.003)P$, where the P is in kPa and c_S is in $\mathrm{g/m^3}$ over the temperature range of $24 \pm 1\,^{\circ}\mathrm{C}$ based on the molar Henry's law constants for nitrogen, oxygen, and argon molecules dissolved in fresh water. The uncertainty in the calculated saturation concentration difference based on the nominal throat pressure is $(c_0 - c_S) \pm 4\%$. Note that we are using mass densities for the gas concentration.

Air was injected at the apex of the wedge to validate the measurement of the gas flux, as discussed below. The air was metered

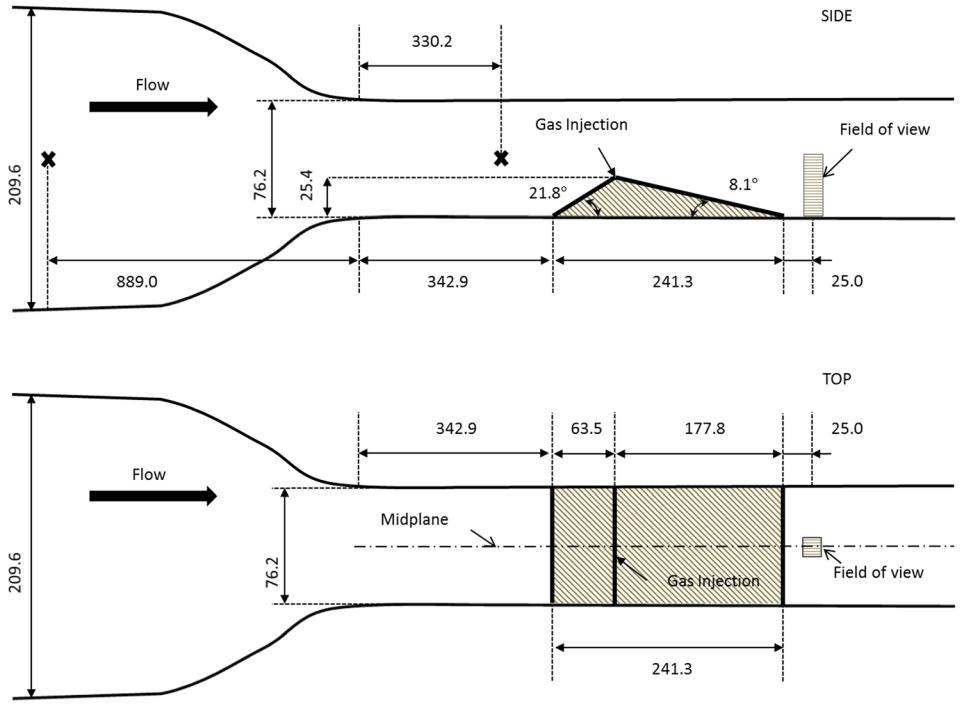

Fig. 2 Top and side schematic views of the wedge in the test section of the water channel. All dimensions are in millimeters. An "X" indicates locations of the pressure taps used to measure the freestream pressure, *P*, and average flow velocity, *U*. The fields of view for visualizing the bubbly wake behind the cavity are also shown.

using a mass flow meter (Omega FMA 6707), and the mass flux of air was known to have an uncertainty of $\pm 2.0 \times 10^{-4}$ g/s at 24 °C.

Void Fraction Measurements Using X-Ray Densitometry. The void fraction of the partial cavity was measured using a two-dimensional time-resolved X-ray densitometry system described in detail by Mäkiharju et al. [10]. A fan beam of X-rays from a 150 kV 433 mA source passed through the measurement domain, wherein it is attenuated according to the Beer–Lambert law. After the measurement domain, the beam encounters a two-dimensional imager consisting of an X-ray image intensifier coupled to a high-speed camera. The light intensity distribution measured by the camera can then be related back to a spanwise-averaged projection of the void fraction in the measurement domain. The uncertainty in the time-average cavity void fractions presented below is ±1% in average void fraction.

Measurement of Bubble Populations in Cavity Wake. Bubble populations were measured downstream of the cavity using a high-magnification imager coupled to a high-speed digital video camera. A Phantom V710 camera was used with a Questar, QM 100 Photo-Visual Long Distance microscope as a high-magnification imager. This coupled system was fixed on a stage that could be translated in three directions (flow direction, vertical direction, and spanwise direction). Target was backlit with ARRI, light (ARRILUX 400) lighting system. Videos were taken at six different vertical (cross stream) locations from the bottom flow boundary with 8 mm interval, focusing at the center plane in depth direction at fixed distance 2.5 cm from the wedge. Videos were taken with 800×600 pixel resolution, 13,000 fps of sampling rate, 1–5 μs of exposure time, and 2 s of acquisition time. The depth of field of the imaging volume was determined by traversing a target across the focal plane. The image came into focus over a thickness of 320 μm, as defined by the thickness over which a sharp boundary of a target plate was in focus.

Figure 3 shows a schematic of the camera setup and the processing parameters. From the video, nonconsecutive images were chosen such that the images did not contain the same bubbles (e.g., they were not correlated). Chosen images were converted to gray scale and median filtered. Mean image through whole video was subtracted from filtered images in order to remove the background. Using edge detecting, the edge of the bubbles was determined. Detected bubbles were sorted by their mean intensity, size, eccentricity, and distance of their centroid from the edge of the image to discard bubbles clipped at the edges. The diameter of the filtered bubble is the average of distances between edge of the bubble in x, y, and two diagonal directions. Image processing was performed using a routine in MATLAB.

To estimate the size of the bubble, images of resolution target were taken with the system to calibrate the size of a pixel (2.9 μm/pixel). Bubbles were counted only when they were equivalent or bigger than 2×2 pixels. Hence, the minimum resolvable bubble size (diameter) was 5.8 μm. The bubble velocity was assumed to be equal to flow velocity. Bubbles were chosen randomly in the video, and their velocities were calculated by computing the bubble displacement for a fixed time period (e.g., the frame rate). At least ten bubbles were selected and each tracked through four to six consecutive frames to determine their average velocity. The estimated uncertainty in the bubble displacement is ±9 μm, and the estimated uncertainty in the bubble phase average velocity is ±0.2 m/s.

The gas volume fraction at the imaging location was estimated after estimating in-focus volume of the image to be 1.25 mm^3, taking the depth of field of the image to be 320 μm. The gas volume was estimated after measuring the diameter of bubble. We assume that: (1) the detected bubbles are spheres and (2) only the portion of the volume inside the focused volume contributes to the volume fraction. The average void fraction in the wake, α_W, is then given by the total gas volume divided by the in-focus measurement volume. As we will discuss below, we will introduce a correction factor to match the measured to the known gas injection fluxes.

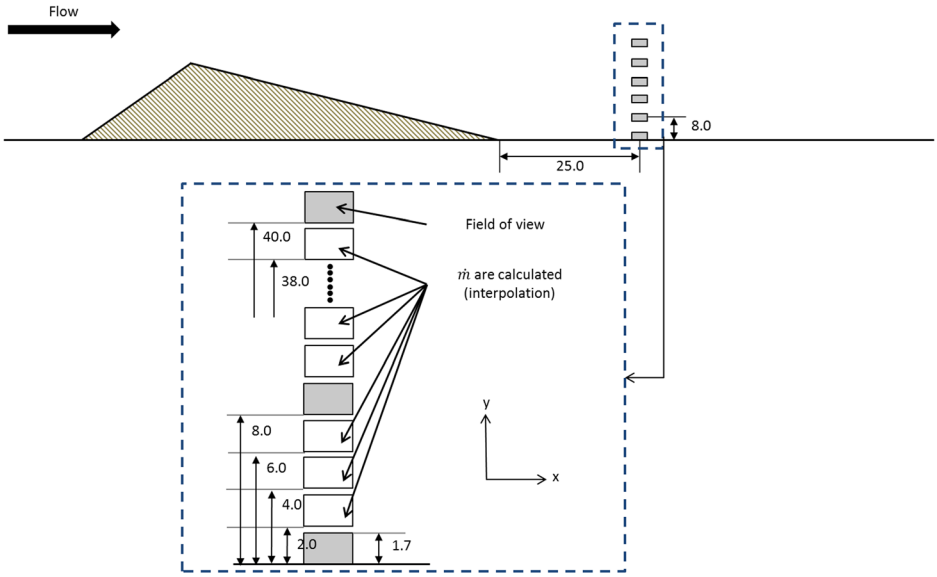

Fig. 3 A detailed view of the fields of view used to determine the void fraction profiles in the wake of the wedge. All dimensions are in millimeters.

Results

Gas Mass Flux in the Wake Due to Injected Air Into the Cavity. In order to validate the optical measurement of the gas flux behind the cavity, a known mass flux of air, $\dot{m}_{\mathrm{INJ}}$, was injected into the wedge apex under noncavitating conditions. The mass flux on the gas downstream of the cavity, $\dot{m}_B$, was determined using the optical measurements by: (1) measuring the bubble populations and mean bubble speeds at six measurements locations above the bottom wall of the test section, (2) determining the local void fraction at each location, and (3) determining the noncondensable mass flux after correcting for the local static pressure, Laplace pressure, and the percentage of water vapor in the bubble, such that

$$\dot{m}_B = \int \alpha_w(y)\rho U(y) W dy \tag{7}$$

The pressure of the noncondensable gas within each bubble of radius R_B is given by

$$P_{Go} = P_W - P_V + \frac{2S}{R_B} \tag{8}$$

where P_W is the static pressure in the measurement location downstream of the wedge and S is the surface tension. The mass of the noncondensable gas in each single bubble is then

$$m_{\mathrm{SB}} = \frac{4}{3}\pi R_B^3 \frac{P_{Go}}{\mathrm{R}T} \tag{9}$$

where R is the ideal gas constant (assumed to be that for air) and T is the temperature. Note that the pressure in the measurement location downstream of the wedge has recovered to well above the vapor pressure, and the bubbles are largely composed of noncondensable gas.

Figure 4 presents the time-averaged void fraction in the wake, noncondensable mass fraction, and gas-phase velocity profiles downstream of the wedge for two cases of gas injection without cavitation. Both data sets were curve fit to provide analytical expressions that could be integrated to determine the gas volume flux. The void fraction profile was fit with a lognormal distribution, and the velocity was fitted with a power-law profile. Figure 5 shows the bubble size distributions. Table 1 shows the results from two gas injection experiments, where $\langle R_B \rangle$ is the average bubble radius and α_W is the average void fraction in the wake. In each case, the optical measurement of the void fraction and resulting gas flux is overestimated by approximately a factor of three. This is likely due to our method of determining the effective thickness of the measurement volume (e.g., the depth of field) and our assumption of spanwise uniformity. In the following results,

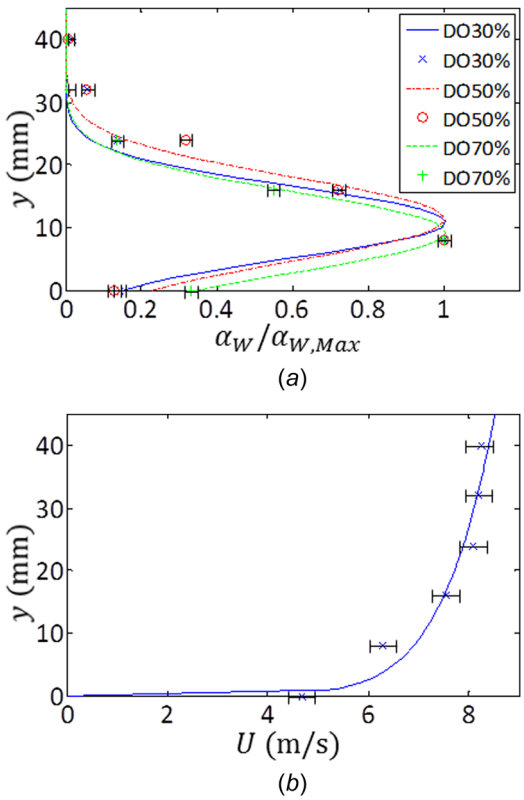

Fig. 4 Profiles of void fraction (*a*) and gas-phase velocity (*b*) are plotted with error bars and fitted curve. (*a*) Three cases are plotted: DO 30%/$\sigma = 2.4$, DO 50%/$\sigma = 2.3$, and DO 70%/$\sigma = 2.7$. Lognormal fitting is used. (*b*) The average velocity on each location from all cases is used.

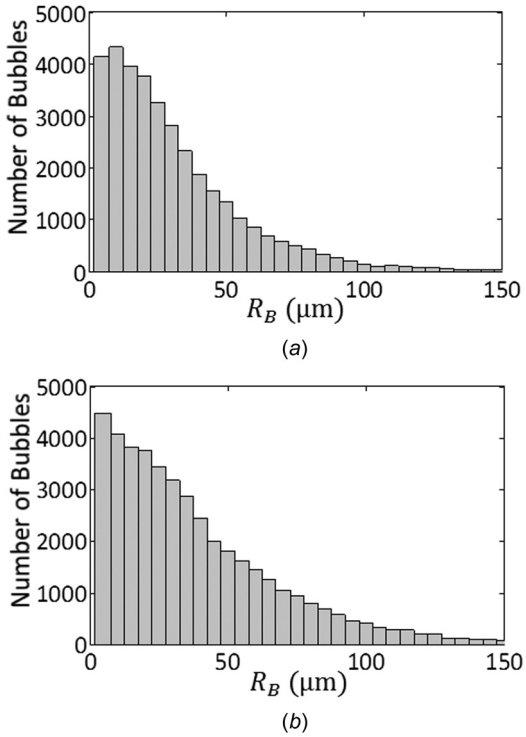

Fig. 5 The measured bubble size distributions for the case of injected air at the wedge apex for injected gas flux of (*a*) 2.5×10^{-3} g/s and (*b*) 6.4×10^{-3} g/s. Data were collected from 6500 independent frames for each case, at $\sigma = 3.4$.

Table 1 Comparison of the injected and measured noncondensable gas flux

σ	$\dot{m}_{\mathrm{INJ}}$ (g/s) $\times 10^3$	$\langle R_B \rangle$ (μm)	$\alpha_W \times 10^4$	$\dot{m}_B$ (g/s) $\times 10^3$	$\dot{m}_B/\dot{m}_{\mathrm{INJ}}$
3.4	2.5	62	6.2	7.2	2.9
3.4	6.4	79	16.0	18.5	2.9

Note: Uncertainties of $\sigma = \pm 0.2$, $\dot{m}_{\mathrm{INJ}} = \pm 2.0 \times 10^{-4}$ g/s, $\langle R_B \rangle = \pm 3\ \mu$m, $\alpha_W = \pm 5\%$, and $\dot{m}_B = \pm 10\%$.

we will reduce the optically measured gas flux produced by the purely cavitating flow by one-third.

Mass Flux of the Noncondensable Gas Diffused Into the Cavity. The gas flux in the wake of the partial cavity was measured without the injection of any air into the cavity. Care was taken to ensure that no noncondensable gas was present in the gas injection system; hence, the bubble populations present downstream of the cavity were comprised of bubbles that may have been present upstream of the cavity and/or bubbles created by dissolution of dissolved gas into the low-pressure zone of partial cavitation near the wedge apex.

Once again, the freestream velocity was fixed at 8 ± 0.2 m/s, but the freestream cavitation number was varied to create partial cavities of different lengths. Figure 6(*a*) shows a photographic image of the cavitating wedge for the case of $L_C = 2.0$ cm corresponding to $\sigma = 2.5$, and Fig. 6(*b*) shows the void fraction field from the X-ray visualization. Note that the average void fraction in the region that could be defined as the cavity based on Fig. 6(*a*) is a few percent.

The cavity length and volume fraction were measured using X-ray densitometry. Note that we are using the X-ray defined cavity length, defined by the extent of the cavity that is greater than 5% void fraction, and the cavity volume is defined as the region that has a greater than 5% void fraction. Figure 7 shows the average cavity length, volume, and void fraction versus cavitation number.

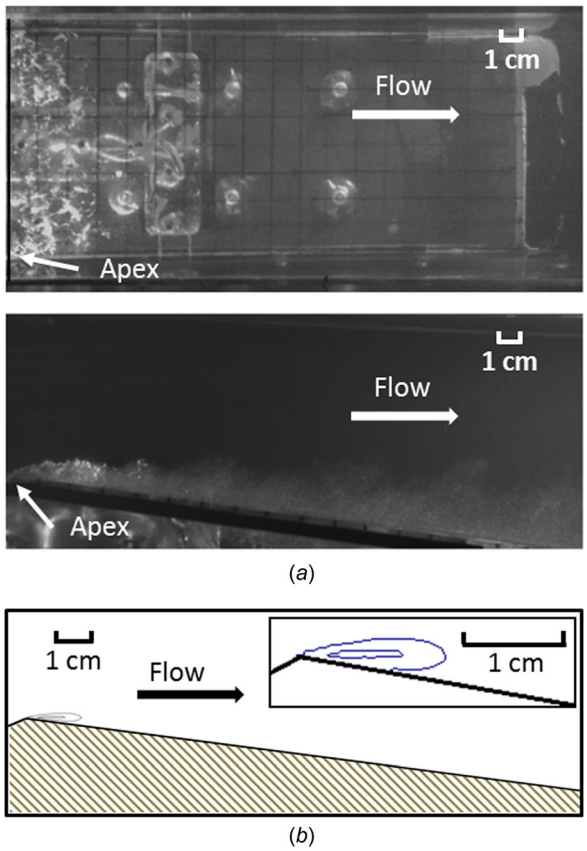

Fig. 6 Both images are cavitating wedge with L_C=2 cm and $\sigma = 2.5$: (*a*) the top and side photographic images and (*b*) the void fraction field for the cavitating flow with an inset showing a close-up of void fraction near the apex. Inner contour is void fraction 15% and outer contour is void fraction 5%.

The average void fractions and cavity lengths based on the curve fits for $3.5 > \sigma > 2$ range from $3\% < \alpha_C < 15\%$ and $0.2 < L_C < 5$ cm.

The bubble populations downstream of the cavities were examined for three different freestream dissolved gas concentrations, c_O, corresponding to oxygen saturation levels of 30%, 50%, and 70% at atmospheric pressure. At the highest pressure ($\sigma = 3.8$), there is no cavitation, and any bubbles measured are part of the background nuclei population. With a reduction in pressure, the cavity forms, and small bubbles can then be observed to persist in the cavity wake, even in the region of pressure recovery downstream of the wedge. Further reduction in pressure corresponds to both an increase in the cavity length and the number of bubbles observed in the cavity wake. Over the range of cavitation numbers tested ($\sigma > 2.0$), the cavity was relatively stable in length (i.e., a closed partial cavity), as compared to a cavity that is shedding large clouds [11].

Figures 8(*a*)–8(*c*) present the bubble size distributions for varying gas saturation, along with the average bubble size. As expected, both the average bubble size and the number of bubbles increase with increasing gas concentration. As before, the velocity and void fraction profiles were curve fitted to allow for integration to determine the void fraction. Table 2 presents the measured results.

The measured gas flux as a function of cavitation number is plotted in Fig. 9. The baseline gas flux due to the freestream nuclei population passing over the wedge is around 7×10^{-7} g/s. With the reduction in freestream pressure and the onset of cavitation, the gas flux increases by three orders of magnitude over the range of cavitation numbers tested. Note the sharp increase in the rate of gas flux when cavity flow changes from undersaturated

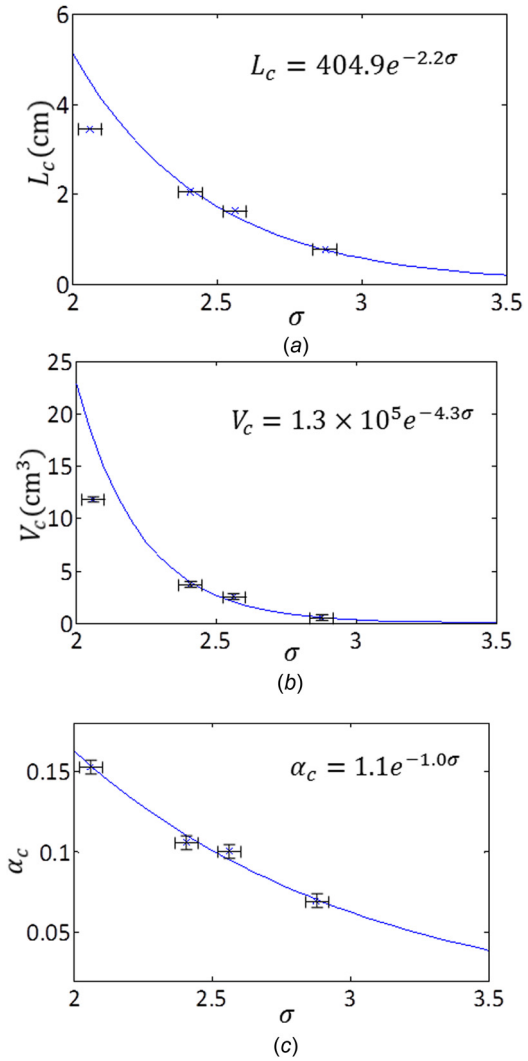

Fig. 7 The average cavity length, L_C (*a*), volume, V_C (*b*), and void fraction α_C (*c*) as a function of cavitation number, σ. The curve fits are also shown that were used to compute values for scaling. (*a*) Uncertainty of average cavity length is ± 0.03 cm.

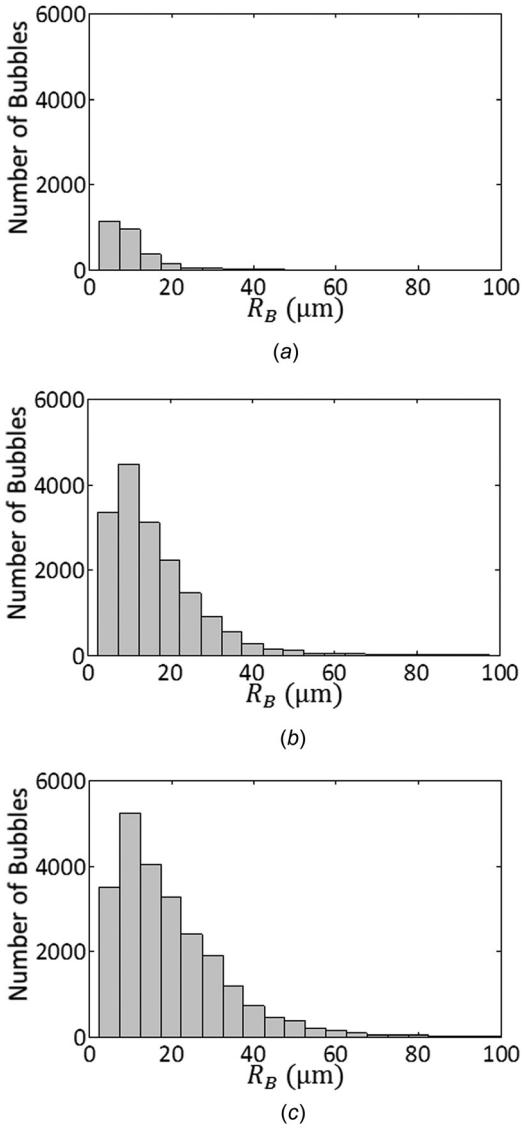

Fig. 8 The measured bubble populations in the cavity wake for DO contents of 30% $\sigma = 2.3$ (*a*), 50% $\sigma = 2.3$ (*b*), and 70% $\sigma = 2.3$ (*c*). Data were collected from 6500 images.

($c_O - c_S < 0$) to supersaturated ($c_O - c_S > 0$) based on the level of saturation in the freestream and the pressure at the apex of the wedge (i.e., the throat pressure). It is interesting to note that there is still outgassing and bubble production even when the average cavity flow is undersaturated, although the rate is much lower compared to the supersaturated conditions. This will be discussed in the "Scaling of the Gas Dissolution Rate" section.

Scaling of the Gas Dissolution Rate

First, the measured gas flux data can be compared to the predicted gas flux from the previous models where the cavity was assumed to be a gas pocket at vapor pressure. Table 3 presents the scaled and measured gas diffusion rates. We compare the models of Parking and Kermeen [5] (with $D = 2 \times 10^{-5}$ cm^2/s), Parkin and Ravindra [7] (with $\delta = 1$ mm to approximate the typical model scale boundary layer thickness), and the slug flow model.

Comparing the cases with supersaturated flow at the cavity interface, the results of Table 3 indicate that laminar diffusion model underpredicts the gas diffusion rate by one order of magnitude, while the models that assume turbulent diffusion at the cavity interface overestimate the gas diffusion by up to two orders of magnitude. These observations are consistent with those of Yu and Ceccio [6], and they motivate a re-examination of the basic scaling assumptions. Moreover, the data presented in Fig. 9 illustrate that the gas flux increases nonlinearly with cavitation number, while these models predict a much slower rate of increase with decreasing cavitation number.

It is clear from the void fraction measurements that the mean cavity void fraction is much less than unity for these flows and a free surface does not exist at the cavity interface. Hence, gas diffusion is not taking place at a stratified gas–liquid interface, but within a low-pressure bubbly zone. We therefore expect that we must include the cavity void fraction, α_C, in the scaling.

The cavity is a recirculating bubbly mixture, with freestream fluid continually being entrained and expelled in the cavity wake. Bubbles within the cavity region grow via gas diffusion as they reside in the low-pressure regions where the flow is locally supersaturated, and then, they are expelled from the cavity as the bubbly flow is entrained in the cavity closure. We first consider the gas diffusion rate in a single bubble, $\dot{m}_{SB}$, in the recirculating zone. The rate of ingassing into an individual bubble is scaled by the following relation, following that of Epstein and Plesset [12]:

$$\dot{m}_{SB} = 4\pi D R_{BC}^2 (c_O - c_S)/L_{D\delta} \tag{10}$$

Table 2 The measured bubbly noncondensable gas flux in the cavity wake from natural cavities for varying cavitation number and DO content

DO%	σ	L_C (cm)	$\alpha_C \times 10^2$	$c_O - c_S$ (g/m^3)	No. of bubbles	$\langle R_B \rangle$ (μm)	$\alpha_W \times 10^6$	$\dot{m}_B$ (g/s) $\times 10^7$
30	**3.0**	**0.6**	**6.5**	**−5.9**	**459**	**18**	**0.05**	**2**
30	**2.7**	**1.1**	**8.5**	**−3.9**	**564**	**16**	**0.10**	**5**
30	**2.4**	**2.1**	**11.1**	**−1.9**	**2534**	**19**	**0.61**	**27**
30	**2.3**	**2.6**	**12.1**	**−1.2**	**2661**	**19**	**0.70**	**31**
50	**3.0**	**0.6**	**6.3**	**−1.4**	**429**	**16**	**0.04**	**2**
50	2.7	1.1	8.5	0.8	2923	18	0.61	27
50	2.3	2.4	11.7	2.8	11,534	27	9.67	423
50	2.3	3.0	12.8	3.5	16,705	32	24.8	1064
70	3.3	0.3	4.8	1.2	252	16	0.07	3
70	3.0	0.7	6.7	3.7	2749	19	0.61	26
70	2.7	1.2	8.7	5.7	9575	25	6.12	249
70	2.3	2.4	11.7	8.5	23,537	39	67.4	2805

Note: The number of bubbles is measured in the field of view for 2 s. The gas flux measured for the undersaturated cases is shown in bold. Uncertainties of DO = ±2%, $\sigma = \pm 0.2$, $L_C \pm 0.3$ mm, $\alpha_C \pm 0.1$, $c_0 - c_S = \pm 4\%$, $\langle R_B \rangle = \pm 3\mu$m, and $\alpha_W = \pm 5\%$. The confidence interval of the measured gas flux is $0.5\,\dot{m}_B < \dot{m}_B < 2\dot{m}_B$.

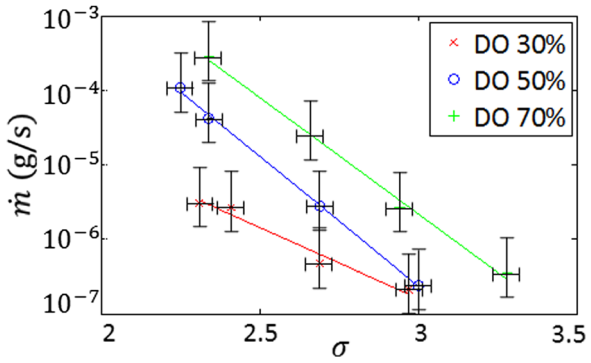

Fig. 9 The measured net gas flux, $\dot{m}_B$, produced as a result of diffusion into the partial cavity as a function of cavitation number, σ. The uncertainty shown in $\dot{m}_B$ spans between two times and 0.5 times the values measured. Results for three DO contents are shown.

where R_{BC} is the average bubble radius within the cavitating region and $L_{D\delta}$ is a length scale related to the local diffusion boundary layer at the bubble surface. The saturation concentration, c_S, is evaluated at the average cavity throat pressure that was estimated using the Bernoulli equation and average flow velocity through the contraction at the wedge apex (12 m/s). The total mass flux of gas coming out of solution in the cavity, $\dot{m}_B$, is related the number of bubbles in the cavitating region defined as

$$N_B = \alpha_C V_C / \frac{4}{3}\pi R_{BC}^3 \tag{11}$$

where α_C is the average cavity void fraction and V_C is the cavity volume. Thus, the net mass flux of gas out of the cavity will be given by

$$\dot{m}_{B,Sat} = \dot{m}_{SB} N_B = \frac{3\alpha_C V_C D(c_O - c_S)}{R_{BC} L_{D\delta}} \tag{12}$$

Note that $3\alpha_C V_C / R_{BC}$ is the interfacial area of the bubbles within the cavity. Interestingly, the flow speed over the cavity does not appear directly in this scaling, since the flux of liquid in and out of the cavity would increase with increasing speed, while the residence time for bubbles in the cavity will decrease with increasing speed. However, increase in the flow speed will likely change the diffusion processes in the cavity, as the diffusion boundary layers on the bubble may thin and the bubble sizes may change. As the cavitation number decreases, the cavity volume, void fraction, and concentration difference all increase. Hence, this scaling yields an exponential growth in the gas diffusion, as observed in the measured bubble populations.

We can modify this scaling for the cases when the cavity flow is on average undersaturated, based on the average throat pressure. For limited cavities, there is still a suction peak near the position of flow separation at the wedge apex. Therefore, there may be a local portion of the cavity volume that is, on average, supersaturated. Then, the scaling would be appropriate for a smaller portion of cavity volume near the suction peak. Alternatively, we could

Table 3 The measured gas flux, $\dot{m}_B$, and scaled gas flux from natural cavities for varying cavitation number and DO contents, employing the previously proposed scaling models; U_C=12 m/s and δ=1 mm

DO%	σ	L_C (cm)	$c_O - c_S$ (g/m^3)	$\dot{m}_B$ (g/s) $\times 10^7$	$\dot{m}_{BPK}$ (g/s) $\times 10^7$	$\dot{m}_{BB}$ (g/s) $\times 10^7$	$\dot{m}_{BPR}$ (g/s) $\times 10^7$	$\dot{m}_{BSF}$ (g/s) $\times 10^7$
30	**3.0**	**0.6**	**−5.9**	**2**	**−146**	**−19,100**	**−24,100**	**−54,000**
30	**2.7**	**1.1**	**−3.9**	**5**	**−131**	**−17,100**	**−21,700**	**−35,600**
30	**2.4**	**2.1**	**−1.9**	**27**	**−86**	**−11,300**	**−14,300**	**−17,300**
30	**2.3**	**2.6**	**−1.2**	**31**	**−62**	**−8080**	**−10,200**	**−11,200**
50	**3.0**	**0.6**	**−1.4**	**2**	**−34**	**−4500**	**−5690**	**−13,200**
50	2.7	1.1	0.8	27	27	3470	4390	7220
50	2.3	2.4	2.8	423	137	17,900	22,600	25,600
50	2.3	3.0	3.5	1064	188	24,600	31,100	31,700
70	3.3	0.3	1.2	3	22	2850	3600	11,300
70	3.0	0.7	3.7	26	94	12,300	15,600	33,800
70	2.7	1.2	5.7	249	198	25,900	32,800	52,100
70	2.3	2.4	8.5	2805	387	50,700	64,200	72,500

Note: The gas flux measured for the undersaturated cases is shown in bold. "PK," "B," "PR," and "SF" refer to the models of Refs. [5], [2], and [7], and the slug flow model [7], respectively. The confidence interval of the measured gas flux is $0.5\dot{m}_B < \dot{m}_B < 2\dot{m}_B$.

Table 4 The measured and scaled gas flux from natural cavities for varying cavitation number and DO content, employing the proposed scaling models for saturated and undersaturated conditions

DO%	σ	V_C (m^3) $\times 10^6$	$\alpha_C \times 10^2$	$c_O - c_S$ (g/m^3)	$\dot{m}_B$ (g/s) $\times 10^7$	$\dot{m}_{B,\mathrm{USat}}$ (g/s) $\times 10^7$	$\dot{m}_{B,\mathrm{Sat}}$ (g/s) $\times 10^7$	$\frac{\dot{m}_B}{\dot{m}_{B,\mathrm{Scaled}}}$
30	**3.0**	**0.4**	**6.5**	**−5.9**	**2**	3		**0.7**
30	**2.7**	**1.2**	**8.5**	**−3.9**	**5**	9		**0.5**
30	**2.4**	**4.0**	**11.1**	**−1.9**	**27**	19		**1.4**
30	**2.3**	**6.0**	**12.1**	**−1.2**	**31**	23		**1.3**
50	**3.0**	**0.3**	**6.3**	**−1.4**	**2**	20		**0.1**
50	2.7	1.2	8.5	0.8	27		66	**0.4**
50	2.3	5.2	11.7	2.8	423		1436	**0.3**
50	2.3	7.8	12.8	3.5	1064		2916	**0.4**
70	3.3	0.1	4.8	1.2	3		5	**0.8**
70	3.0	0.4	6.7	3.7	26		83	**0.3**
70	2.7	1.4	8.7	5.7	249		565	**0.4**
70	2.3	5.2	11.7	8.5	2805		4073	**0.7**

Note: The gas flux measured for the undersaturated cases is shown in bold. The confidence interval of the measured gas flux is $0.5\dot{m}_B < \dot{m}_B < 2\,\dot{m}_B$. Uncertainties of $\dot{m}_{B,\mathrm{USat}}$ and $\dot{m}_{B,\mathrm{Sat}}$ are both $\pm 11\%$ for the given underlying scaling constants assumed.

employ the true average cavity under pressure, which would include the suction peak, and this might produce supersaturated average conditions even at the higher cavitation numbers. In the present work, we will use a modified scaling based on the average throat pressure and a finite cavity volume smaller that the total volume

$$\dot{m}_{B,\mathrm{USat}} = \frac{3\alpha_C V_{C,\mathrm{US}} D(c_O - c_{S,\mathrm{US}})}{R_{\mathrm{BC}} L_{D\delta}} \tag{13}$$

where the subscript "US" denotes the undersaturated condition when $(c_O - c_S) < 0$ for the average cavity pressure, but $(c_O - c_{S,\mathrm{US}}) > 0$ in the low-pressure region near the cavity separation. In this scaling, the void fraction and the level of supersaturation will increase with decreasing cavitation number, but the portion of the cavity volume where outgassing occurs would remain relatively constant, even with decreases in pressure. Hence, the rate of mass diffusion would increase with decreasing cavitation number, but at a much lower rate, as observed for the cases where $(c_O - c_S) < 0$.

To perform the scaling, we must make some assumptions. First, we assume that the average bubble radius in the cavity is of order $R_{\mathrm{BC}} \sim 100\ \mu$m. This is a value in the range as reported in Ref. [13]. The diffusion length scale increases as $L_{D\delta} \sim \sqrt{\pi D t}$, and if we assume a residence time on the order of a few millisecond (which is on the order of L_C/U_C), then $L_{D\delta} \sim 10\ \mu$m. For the undersaturated cases, we will assume that the local suction peak leads to a pressure that is about half the average throat pressure and that the volume with the reduced pressure extends about 1 cm from the wedge apex.

Table 4 shows the scaled and measured gas fluxes as a function of cavitation number after employing these assumptions. The raw scaling predicts gas flux that is on the order of that of the observed values, but the effective scaling factor can be changed with changes in the assumed average bubble size in the cavity, the diffusion length scale, or other model parameters. More importantly, the scaling successfully captures nonlinear increase in gas flux with lowering of the cavitation number, and this trend suggests that the basic physical reasoning behind the proposed scaling is valid.

Conclusions

We have shown that the significant quantities of noncondensable gas bubbles can be produced in the wake of a partial cavity as a result of outgassing into the low-pressure cavitating region. Previously proposed scalings for this process have been offered that are based on the presence of a free surface at the cavity interface. However, the cavities under consideration here are not gas pockets but are, instead, bubbly mixtures. A new scaling has been proposed that captures the order of magnitude of the gas flux due to diffusion into the bubbly flow, along with the strong change in mass diffusion as a result of changing flow parameters (i.e., the cavitation number and dissolved gas content). This scaling is based on the average properties of the bubbly cavitating flow. However, we found that net outgassing was observed, even when the flow in the cavitating region was, on average undersaturated. We accounted for this by assuming that there may be a local region of strongly negative pressure near the cavity suction peak that leads to outgassing. Therefore, improved scaling may be devised which takes into account the flow structure of the local cavity flow where both the mean and unsteady pressures may be much lower than the average cavity pressure, such as in the cavitating shear layer at the point of cavity detachment.

Acknowledgment

This work was supported by the Office of Naval Research under Grant No. N00014-10-1-0974, Dr. Patrick Purtell, and the National Research Foundation of Korea (NRF) under Grant No. N014691.

Nomenclature

c_O = freestream dissolved gas concentration (g/m^3)
c_S = saturated dissolved gas concentration at the cavity surface (g/m^3)
$c_{S,\mathrm{US}}$ = saturated dissolved gas content at the cavity surface in the low-pressure region near the cavity separation (g/m^3)
D_t = molecular mass diffusion coefficient (m^2/s)
k_B = constant used at each model (value varies by assumptions)
L_C = partial cavity length (m)
L_D = length scale derived from each modeling assumptions (m)
L_{DB} = length scale used on model of Brennen [2] (m)
L_{DPK} = length scale used on model of Parkin and Kermeen [5] (m)
L_{DPR} = length scale used on model of Parkin and Ravindra [7] (m)
L_{DSF} = length scale used on slug flow model [7] (m)
$L_{D\delta}$ = length scale related to the diffusion boundary layer at the bubble surface within the cavity (m)
m_{SB} = mass of the noncondensable gas in a single bubble (kg)
$\dot{m}_B$ = net mass flux (kg/s)
$\dot{m}_{B,\mathrm{Sat}}$ = net mass flux in the wake of the cavity for supersaturated conditions (kg/s)
$\dot{m}_{B,\mathrm{USat}}$ = net mass flux in the wake of the cavity for undersaturated conditions (kg/s)

$\dot{m}_{INJ}$ = mass flux of air injected into wedge apex (kg/s)
$\dot{m}_{SB}$ = mass rate of ingassing into a single bubble (kg/s)
N_B = number of bubble
P = static pressure in the measurement location upstream of the wedge (kPa)
P_T = throat pressure (kPa)
P_V = liquid vapor pressure (kPa)
P_W = static pressure in the measurement location downstream of the wedge (kPa)
P_{Go} = pressure of the noncondensable gas in a bubble (kPa)
R = ideal gas constant of air (kJ/kg K)
R_B = bubble radius measured in the cavity wake (m)
R_{BC} = average bubble radius within the cavitating region (m)
$\langle R_B \rangle$ = average bubble radius measured in the cavity wake (m)
S = surface tension of water against air (N/m^2)
S_C = Schmit number ($S_C = \nu/D$)
S_{C_t} = turbulent Schmit number ($S_{C_t} = \nu/D_t$)
T = temperature (K)
t_B = residence time of the bubbles in supersaturated region pressure (s)
U = freestream average flow speed (m/s)
U_C = flow speed at the cavity interface (the throat speed) (m/s)
V_C = volume of the partial cavity (m^3)
$V_{C,US}$ = volume of the partial cavity for undersaturated flow (m^3)
W = model span (m)
α_C = average void fraction of partial cavity
α_W = average void fraction in the wake
δ = boundary layer thickness of the flow at the cavity interface (m)
θ = momentum thickness of the flow at the cavity interface (m)
ρ = liquid density (kg/m^3)
σ = cavitation number $\left(\sigma = \frac{P-P_V}{\frac{1}{2}\rho U^2}\right)$
υ = liquid kinematic viscosity (m^2/s)

References

[1] Billet, M. L., and Weir, D. S., 1975, "The Effect of Gas Diffusion on the Flow Coefficient for a Ventilated Cavity," ASME J. Fluids Eng., **97**(4), pp. 501–506.
[2] Brennen, C. E., 1969, "The Dynamic Balances of Dissolved Air and Heat in Natural Cavity Flow," J. Fluid Mech., **37**(1), pp. 115–127.
[3] Gadd, G. E., and Grant, S., 1965, "Some Experiments on Cavities Behind Disks," J. Fluid Mech., **23**(4), pp. 645–656.
[4] Maeda, M., Yamaguchi, H., and Kato, H., 1991, "Laser Holography Measurement of Bubble Population in Cavitation Cloud on a Foil Section," Cavitation '91 Symposium, FED-Vol. **116**, pp. 67–75.
[5] Parkin, B. R., and Kermeen, R. W., 1962, "The Roles of Convective Air Diffusion and Liquid Tensile Stresses During Cavitation Inception," I.A.H.R. Symposium on Cavitation and Hydraulic Machinery, Sendai, Japan, Sept. 3–8, pp. 21–24.
[6] Yu, P.-W., and Ceccio, S. L., 1997, "Diffusion Induced Bubble Populations Downstream of a Partial Cavity," ASME J. Fluids Eng., **119**(4), pp. 782–787.
[7] Parkin, B. R., and Ravindra, K., 1991, "Convective Gaseous Diffusion in Steady Axisymmetric Cavity Flows," ASME J. Fluids Eng., **113**(2), pp. 285–289.
[8] Coutier-Delgosha, O., Stutz, B., Vabre, A., and Legoupil, S., 2007, "Analysis of Cavitating Flow Structure by Experimental and Numerical Investigations," J. Fluid Mech., **578**, pp. 171–222.
[9] Stutz, B., and Legoupil, S., 2003, "X-Ray Measurements Within Unsteady Cavitation," Exp. Fluids, **35**(2), pp. 130–138.
[10] Mäkiharju, S. A., Chang, N., Gabillet, C., Paik, B.-G., Perlin, M., and Ceccio, S. L., 2013, "Time-Resolved Two-Dimensional X-Ray Densitometry of a Two-Phase Flow Downstream of a Ventilated Cavity," Exp. Fluids, **54**(7), pp. 1561–1582.
[11] Laberteaux, K. R., and Ceccio, S. L., 2001, "Partial Cavity Flows. Part 1. Cavities Forming on Models Without Spanwise Variation," J. Fluid Mech., **431**, pp. 1–41.
[12] Epstein, P. S., and Plesset, M. S., 1950, "On the Stability of Gas Bubbles in Liquid–Gas Solutions," J. Chem. Phys., **18**(11), pp. 1505–1508.
[13] Coutier-Delgosha, O., Devillers, J.-F., Pichon, T., Vabre, A., Woo, R., and Legoupil, S., 2013, "Internal Structure and Dynamics of Sheet Cavitation," Phys. Fluids, **18**, pp. 1–12.